



Vibration analysis of nonlinear damping systems by the discrete incremental harmonic balance method

Sheng Wang · Yongou Zhang · Wenyong Guo · Ting Pi · Xiaofeng Li

Received: 23 November 2021 / Accepted: 27 September 2022 / Published online: 11 October 2022
© The Author(s), under exclusive licence to Springer Nature B.V. 2022

Abstract An improved incremental harmonic balance method (IHBM) is proposed by Wang (J Sound Vib 441:111–125, 2019) to solve the periodic responses of the continuous nonlinear stiffness systems. However, the nonlinear damping systems remain unsolved. This paper aims to investigate the nonlinear damping parts by the proposed IHBM method, which is based on the principle that any continuous curve can be approximated by a piecewise-linear curve with discrete nodes. The piecewise-linear function can be considered a unified benchmark function that can convert the complex IHBM Galerkin process of arbitrary nonlinear damping systems to that of unified piecewise-linear damping systems. The general process of the proposed method for this piecewise-linear system is derived considering the stability of the solutions. Then, a polynomial nonlinear damping system is investigated to validate the accuracy of the method. Furthermore, five typical cases of single-degree-of-freedom (SDOF) nonlinear damping systems are carried out, and this method is also extended to multi-degree-of-freedom (MDOF)

systems where each nonlinear force in the systems is expressed by the function of only one independent DOF. The results illustrate that the proposed method shows convenience and accuracy in obtaining the dynamics of nonlinear systems.

Keywords Incremental harmonic balance method · Discrete node process · Equivalent piecewise-linearization · Nonlinear damping system · Hysteretic system

1 Introduction

Modern mechanical design usually includes steps from functional design to performance design. Among the performance designs, vibration and noise reduction has become the core of many products. However, certain designs for suppressing vibration and noise are based on linear system designs that cannot distinguish output characteristics under different inputs. Therefore, control techniques that not only increase the cost but also reduce the system's reliability are introduced. The nonlinear system, on the other hand, can meet the need of the above performance designs with its own characteristics and can be regarded as a direct, passive vibration controller. Consequently, the application of nonlinear components, including inertial, stiffness and damping devices, in mechanical products has gradually expanded, and nonlinear designs and

S. Wang (✉) · W. Guo · T. Pi · X. Li
College of Power Engineering, Naval University of Engineering, Wuhan 430033, China
e-mail: wangsheng_tao@outlook.com

Y. Zhang (✉)
School of Transportation, Wuhan University of Technology, Wuhan 430070, China
e-mail: zhangyo@whut.edu.cn

corresponding analysis have become mainstream directions for mechanical designs.

There are numerous mechanisms that employ geometry nonlinearity that can be regarded as passive isolators to improve the performance of vibration reduction [1–4]. However, the phenomena of the amplitude jump in primary resonance and subharmonic/supharmonic responses introduced by the nonlinear stiffness may cause new problems for the isolators' performance [5, 6]. Thus, nonlinear damping devices are considered to suppress the resonance amplitudes of nonlinear systems and avoid the above shortcomings. The most classical nonlinear damping is cubic damping, which is an effective way to reduce vibrational amplitude among large velocity regions [7]. Xiao [8] analyzed a nonlinear vibrator that contained cubic damping and stiffness by the output frequency response function. The analytical results showed that cubic damping could provide better performance for vibration isolators under force excitation or base displacement excitation. Other polynomial types of nonlinear damping include fluid damping expressed by the square velocity mathematical model, higher-order polynomial damping [9], and velocity & displacement-dependent damping (VDD) [10]. Another representative type of nonlinear damping is dry friction damping, which is considered in cases caused by the unavoidable contact with the relative interface velocity between each element of the isolator [5]. Different models, such as Coulomb damping [11], have been proposed. The Coulomb model can evolve diverse models which are closer to reality [12], such as the continuous model that considers elastic connection between the mass and the contact surface [13]. Furthermore, the Coulomb model can be developed into the hysteretic model that refers to the lagging effect caused by material nonlinearity. Typical hysteretic models include the algebraic model and differential model [14–16]. The former, such as the bilinear model, utilizes an algebraic equation to compute the output parameters, while the latter can be described by differential models, such as the Bouc–Wen model. The dynamics of the bilinear model under period excitations are investigated by Caughey [17] via the perturbation method. This model can be considered as a simplified hysteretic model while its dynamics are complicated due to the switches to various modes [18, 19]. The Bouc–Wen model is widely analyzed due to the

perfect mathematical expressions [20, 21]. Vaiana [15, 16] studied class of uniaxial symmetric rate-independent models to simulate complex asymmetric mechanical hysteresis phenomena. However, there are hardly universal methods of solving these nonlinear damping models.

Many methods, such as the equivalent-linear method [22, 23], averaging method [10], and harmonic balance method (HBM) [24, 25], are adopted to investigate the dynamics of nonlinear systems. These methods may face some problems involving various nonlinear systems. For example, the computation errors would be relatively large for systems with strong nonlinearity, and immense derivation efforts will be made for MDOF nonlinear systems or systems with hysteretic models. To overcome these difficulties, Lau and Cheung [26] combined the HBM with the incremental method, and the incremental harmonic balance method was proposed to address MDOF systems or strongly nonlinear systems. However, the classical IHBM [27–29] has two shortcomings: (1) the universality problem, in which it is difficult to construct a unified form for the derivation of different types of nonlinear terms; (2) the derivation problem, since it is suitable for specific forms of nonlinear systems such as polynomial or piecewise-linear types while other types require much more complicated derivations or cannot be solved. In view of the above problems, one common way is to replace or approximate the Galerkin process, which is the most complicated derivation process. Wang [30] improved the IHBM with the fast Fourier transform and Broyden's method to reduce the derivation complexity. Kong [3] and Sun [31] employed the multiterm IHBM to address the piecewise-nonlinear system by a discrete Fourier transform. The Taylor series are applied to approximate the complicated expressions of linear guide of the ball bearing with the polynomial functions. Hui [14, 32] added a virtual DOF to the hysteretic model, namely the restoring force into the IHBM procedure to solve the Bouc–Wen model. These attempts are efficient in solving their respective problems and have reduced the amount of derivation of the complex Galerkin process to a certain extent. However, they do not completely solve the problem of algorithm generality, and separate derivations are still needed to solve different types of nonlinear systems.

An alternative way for the above problems is to select a unified basic function to equate various

nonlinear functions to the basic function, and to solve this basic function by the traditional IHBM. Only the Galerkin process of this basic function is essential for the derivation. Based on this idea, the author conducted a study on nonlinear stiffness systems [33]. However, the nonlinear damping systems which consist of material nonlinearity including the hysteretic systems still remain unsolved by the proposed method. In this paper, both nonlinear stiffness and damping are included to construct a universal procedure for obtaining periodic solutions to nonlinear SDOF isolator/absorber or energy harvester systems. Furthermore, the proposed method is extended to the MDOF systems where each nonlinear force in the system is expressed by the function of only one independent DOF. The paper is organized as follows: Sect. 2 introduces the discrete node process by equivalent piecewise-linearization procedure to deal with the nonlinear damping models including the hysteretic models. In Sect. 3, the proposed IHBM is derived together with the stability analysis of the solutions. Section 4 examines the accuracy of the proposed method with nonlinear damping systems. Conclusions are drawn in Sect. 5.

2 Discrete node process for nonlinear damping

2.1 General process

Consider a SDOF, nonlinear damping model with continuous characteristics. The velocity-force characteristics are shown in Fig. 1. $h(v)$ is the original damping force of the system and is replaced by $g(v)$ with discrete nodes A_{-p}, \dots, A_{N-p} that connect end to end with straight lines, which represents the approximate piecewise-linear damping force. w_i denotes the arc length of the original curve segment i , and l_i is the length of straight line segment i .

The equivalent piecewise-linearized error ε (linearized error for short) that is defined in Eq. (1) can be utilized to determine the maximum computation result error between the original system and the equivalent piecewise-linearization system (result error for short). The concept can be analogized to the two-norm.

$$\varepsilon = \sqrt{\frac{1}{N} \left(\sum_{i=-p}^{-1} \left(\frac{w_i}{l_i} - 1 \right)^2 + \sum_{i=1}^{N-p} \left(\frac{w_i}{l_i} - 1 \right)^2 \right)} \quad (1)$$

The main idea is to transform the complex continuous damping into the uniform piecewise-linear damping, and this piecewise-linear damping system can be solved by the IHBM. The discrete number N obtained by node division is relevant to the linearized error. If N approaches infinity, the equivalent system can be treated as the original system as the result error is zero, while the computation time increases unlimitedly. Therefore, it is essential to obtain a proper N to meet the requirement of the computation accuracy and time, and the calibration with the result error is given in Sect. 4.1 by a SDOF polynomial nonlinear damping system.

The discrete node process can be carried on as follows: first, the nonlinear damping curve is divided into N segments by $N + 1$ nodes, namely, $A_{-p}, A_{-p+1}, \dots, A_{-1}, A_0, A_1, \dots, A_{N-p-1}, A_{N-p}$; the node division method can be uniformly spaced, and local refinement can be proceeded depending on the smoothness of the curve. Second, suppose the coordinates of these nodes are $(d_i, h(d_i))$, respectively, where i is the segment number, the slope of the linearized segment can be computed by:

$$c_i = \frac{h(d_i) - h(d_{i-1})}{d_i - d_{i-1}}, c_{-i} = \frac{h(d_{-i}) - h(d_{-i+1})}{d_{-i} - d_{-i+1}} \quad (2)$$

Last, the expression of this equivalent piecewise damping system can be written in the following unified form:

$$\begin{aligned} g(0) &= 0, d_0 = 0, d_{-p} = -\infty, d_{N-p} = \infty \\ g(x) &= c_{-i}(x - d_{-(i-1)}) + h(d_{-(i-1)}), d_{-i} \leq x \leq d_{-(i-1)}, \\ &\quad (i = 1, 2, \dots, p) \\ g(x) &= c_i(x - d_{i-1}) + h(d_{i-1}), d_{i-1} \leq x \leq d_i, \\ &\quad (i = 1, 2, \dots, N-p) \end{aligned} \quad (3)$$

It should be noted that certain discontinuous models, such as the Coulomb dry friction model, can also be made equivalent to continuous models by using polynomial curve fitting techniques [41].

2.2 Particular strategy for hysteresis loops

Section 2.1 discusses the nonlinear damping system which consists of only velocity items. However, this process cannot deal with nonlinear hysteretic systems that contain not only velocity items but also

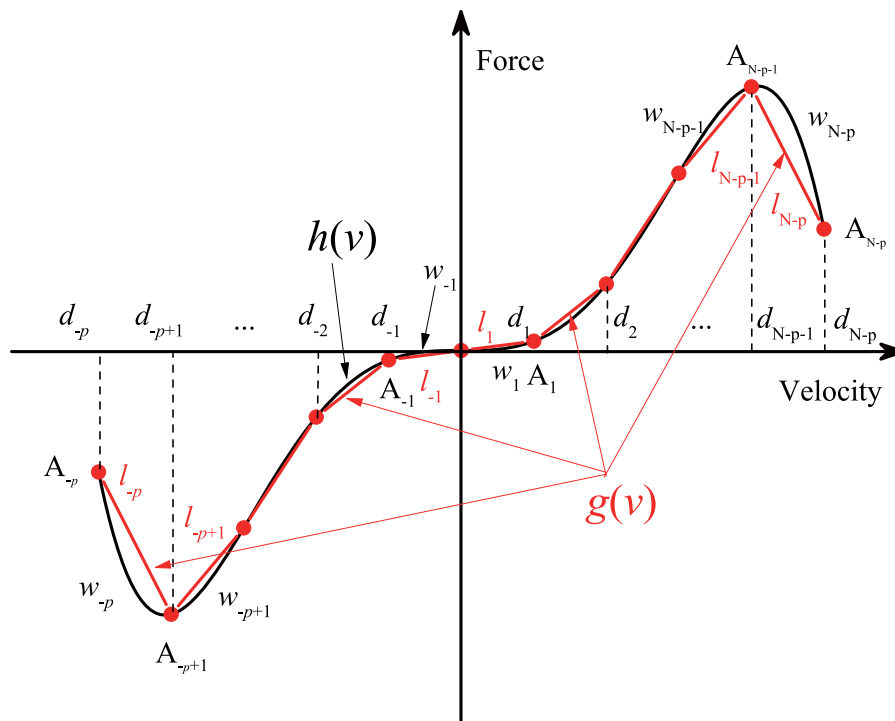


Fig. 1 Discrete node process and piecewise linearization for nonlinear continuous damping

displacement items. In this section the strategy for hysteretic systems is investigated.

We address two typical kinds of hysteretic dampings: the bilinear hysteretic model (shown in Fig. 2a) and Bouc–Wen model (shown in Fig. 2b). The discrete node process can also be applied to these models, and they can be regarded as the same model by the discrete node process. For example, curves \widehat{BCE} and \widehat{EDB} in the Bouc–Wen model can be linearized into piecewise-linear curves that are similar to the corresponding curves in the bilinear model. Therefore, these hysteretic models are degenerated into a unified piecewise-linear form. The whole model can be divided into three parts by point B and point E: curves \widehat{AB} , \widehat{BCE} or \widehat{EDB} and \widehat{EF} , each part can be linearized separately.

By the above process, when the hysteresis loops are obtained by experiments or computed by the mathematical model, the discrete node process can be directly adopted. Additionally, most hysteretic models do not include curves \widehat{AB} and \widehat{EF} , and the parameters y_B/y_E for the model are the output parameters to be calculated. These parameters can be solved by an additional Newton-Rapson interactive method.

3 IHBM scheme with piecewise-linear systems

3.1 Piecewise-linear IHBM scheme

After the above discrete node process, the traditional piecewise-linear IHBM procedure can be applied. Consider a SDOF system with nonlinear damping and stiffness characteristics:

$$\omega^2 \frac{d^2y}{d\tau^2} + 2\xi\omega \frac{dy}{d\tau} + y + h(y) + r(y) = e(\tau) \tag{4}$$

In Eq. (4), τ is the non-dimensional time, ξ is the linear damping ratio, $h(y)$ denotes the nonlinear damping presented in Sect. 2, and $r(y)$ is the nonlinear stiffness, and these two nonlinear terms can be replaced by the piecewise-linear functions $g(y)$ and $q(y)$, respectively. $e(\tau)$ is the external periodic force on the system, which can be written in a trigonometric function combination:

$$e(\tau) = f_0/2 + \sum_{i=1}^n (f_i \cos(i\tau) + g_i \sin(i\tau)) \tag{5}$$

The general scheme of the IHBM for piecewise-linear models is derived here. The first step is the

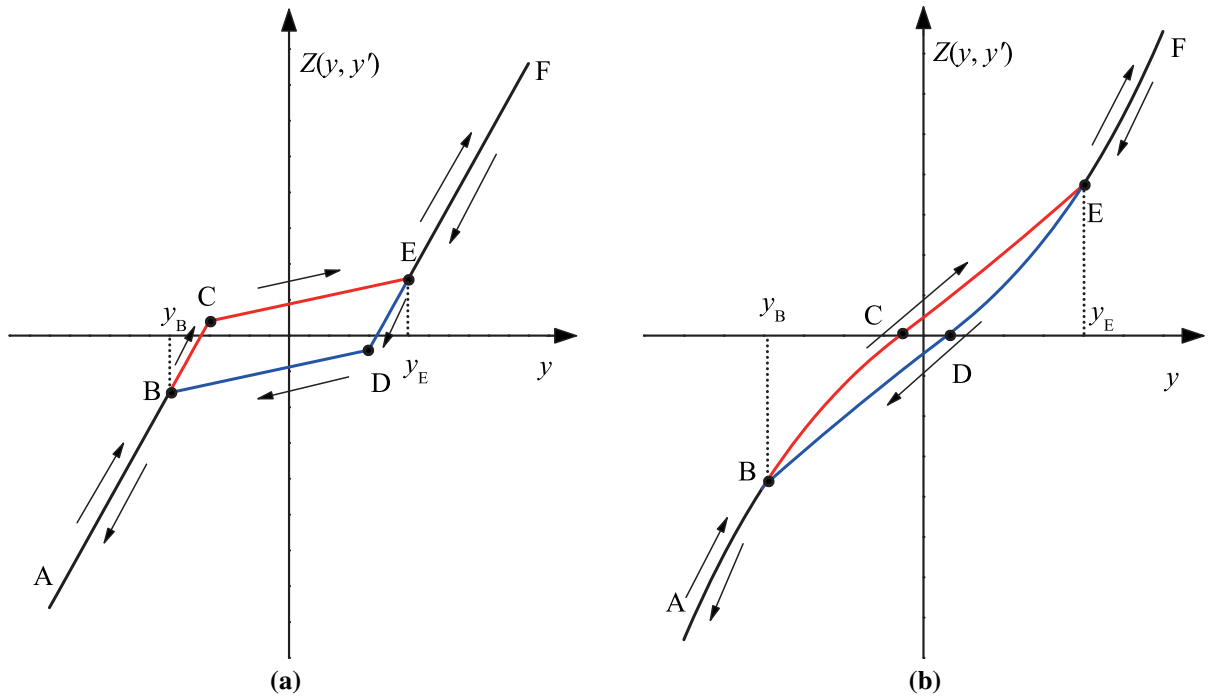


Fig. 2 Hysteresis loop of models: **a** bilinear model; **b** Bouc–Wen model

incremental method. Assuming that the initial state and incremental state of the solution are denoted by parameters y_0, ω_0 and parameters $\Delta y, \Delta\omega$, respectively, the displacement and frequency near the initial state can be expressed as

$$y = y_0 + \Delta y, \quad \omega = \omega_0 + \Delta\omega \tag{6}$$

The incremental procedure is applied by substituting Eq. (6) into Eq. (4), and only the first-order terms of the small increments are considered. The governing equation is expressed as follows:

$$\omega_0^2 \frac{d^2 \Delta y}{d\tau^2} + 2\zeta\omega_0 \frac{d\Delta y}{d\tau} + \Delta y + \frac{\partial g(y)}{\partial y} \Delta y + \frac{\partial q(y)}{\partial y} \Delta y = R + S\Delta\omega \tag{7}$$

where

$$R = - \left[\omega_0^2 \frac{d^2 y_0}{d\tau^2} + 2\zeta\omega_0 \frac{dy_0}{d\tau} + y_0 + g(y_0) + q(y_0) \right] + e(\tau)$$

$$S = -2\omega_0 \frac{d^2 y_0}{d\tau^2} - 2\zeta \frac{dy_0}{d\tau} - \frac{\partial g(y)}{\partial \omega} \Big|_{\omega=\omega_0} \tag{8}$$

As the IHBM can address the period solution of the nonlinear system, the solution can be written in the matrix form:

$$y_0 = \frac{a_0}{2} + \sum_{n=1}^{mH} \left(a_n \cos\left(\frac{n\tau}{m}\right) + b_n \sin\left(\frac{n\tau}{m}\right) \right) = C_s \mathbf{A}$$

$$\Delta y = \frac{\Delta a_0}{2} + \sum_{n=1}^{mH} \left(\Delta a_n \cos\left(\frac{n\tau}{m}\right) + \Delta b_n \sin\left(\frac{n\tau}{m}\right) \right) = C_s \Delta \mathbf{A} \tag{9}$$

where H is the number of fundamental harmonic terms, which is set according to experience in advance, and m is the possible order of the existing subharmonic resonance.

$$C_s = \left[\frac{1}{2}, \cos\left(\frac{\tau}{m}\right), \cos\left(\frac{2\tau}{m}\right), \dots, \cos\left(\frac{mH\tau}{m}\right), \sin\left(\frac{\tau}{m}\right), \sin\left(\frac{2\tau}{m}\right), \dots, \sin\left(\frac{mH\tau}{m}\right) \right]$$

$$\mathbf{A} = [a_0, a_1, \dots, a_{mH}, b_1, b_1, \dots, b_{mH}]^T$$

$$\Delta \mathbf{A} = [\Delta a_0, \Delta a_1, \dots, \Delta a_{mH}, \Delta b_1, \Delta b_1, \dots, \Delta b_{mH}]^T \tag{10}$$

The Galerkin procedure is introduced by substituting Eq. (9) into Eq. (7), and by integrating Eq. (7) from 0 to $2\pi m$. The $2mH + 1$ linearized equations with $2mH + 2$ unknown variables of $\Delta a_n, \Delta b_n$ and $\Delta\omega$ can be acquired in the matrix form:

$$(\mathbf{C}_L + \mathbf{C}_{Nk} + \mathbf{C}_{Nd})\Delta\mathbf{A} = (\mathbf{R}_L + \mathbf{R}_{Nk} + \mathbf{R}_{Nd}) + (\mathbf{S}_L + \mathbf{S}_{Nd})\Delta\omega \tag{11}$$

The elements of the above matrices are derived by adopting the step function proposed by Lau [34]. The expressions of the linear part and piecewise-linear stiffness part of the matrices (namely \mathbf{C}_L , \mathbf{R}_L , \mathbf{S}_L , \mathbf{C}_{Nk} and \mathbf{R}_{Nk}) are derived by Wang [33]. Thus, only the piecewise-linear part of damping matrices is given in this paper.

Assume that $\tau_1, \tau_2, \dots, \tau_Z$ are zeroes of $\dot{y}_0 = d_i$ ($i = -p, \dots, -1, 0, 1, \dots, N - p$), with $\tau_0 = 0$, $\tau_{Z+1} = 2m\pi$, and $t_{1,n}, t_{2,n}, \dots, t_{Z+1,n}$ are sign functions of $\dot{y}_0 - d_n$ ($n = -p - 1, -p, \dots, -1, 0, 1, \dots, N - p + 1$). $G(t_{u,v1}, t_{u,v2})$ can be denoted by:

$$G(t_{u,v1}, t_{u,v2}) = \begin{cases} 1, & t_{u,v1} \cdot t_{u,v2} < 0 \\ 0, & \text{otherwise} \end{cases} \tag{12}$$

Applying sign functions, the piecewise-linear damping part of the matrices can be expressed by:

$$\mathbf{C}_{Nd} = \begin{bmatrix} \mathbf{C}_{11} & \mathbf{C}_{12} \\ \mathbf{C}_{21} & \mathbf{C}_{22} \end{bmatrix}, \mathbf{R}_{Nd} = \begin{bmatrix} \mathbf{R}_1 \\ \mathbf{R}_2 \end{bmatrix}, \mathbf{S}_{Nd} = \begin{bmatrix} \mathbf{S}_1 \\ \mathbf{S}_2 \end{bmatrix} \tag{13}$$

(1) Elements of matrix \mathbf{C}_{Nd} :

$$[\mathbf{C}_{11}]_{ij} = -m\omega_0\alpha_j \sum_{u=0}^Z \left\{ \left[\sum_{v=-p}^{-1} G(t_{u+1,v}, t_{u+1,v+1})c_v + \sum_{v=1}^{N-p} G(t_{u+1,v-1}, t_{u+1,v})c_v \right] \left(B_{ij} \left(\frac{\tau_{u+1}}{m} \right) - B_{ij} \left(\frac{\tau_u}{m} \right) \right) \right\} \tag{14}$$

$$[\mathbf{C}_{12}]_{ij} = -m\omega_0\alpha_i \sum_{u=0}^Z \left\{ \left[\sum_{v=-p}^{-1} G(t_{u+1,v}, t_{u+1,v+1})c_v + \sum_{v=1}^{N-p} G(t_{u+1,v-1}, t_{u+1,v})c_v \right] \left(A_{ij} \left(\frac{\tau_{u+1}}{m} \right) - A_{ij} \left(\frac{\tau_u}{m} \right) \right) \right\} \tag{15}$$

$$[\mathbf{C}_{21}]_{ij} = -m\omega_0\alpha_j \sum_{u=0}^Z \left\{ \left[\sum_{v=-p}^{-1} G(t_{u+1,v}, t_{u+1,v+1})c_v + \sum_{v=1}^{N-p} G(t_{u+1,v-1}, t_{u+1,v})c_v \right] \left(D_{ij} \left(\frac{\tau_{u+1}}{m} \right) - D_{ij} \left(\frac{\tau_u}{m} \right) \right) \right\} \tag{16}$$

$$[\mathbf{C}_{22}]_{ij} = -m\omega_0 \sum_{u=0}^Z \left\{ \left[\sum_{v=-p}^{-1} G(t_{u+1,v}, t_{u+1,v+1})c_v + \sum_{v=1}^{N-p} G(t_{u+1,v-1}, t_{u+1,v})c_v \right] \left(C_{ij} \left(\frac{\tau_{u+1}}{m} \right) - C_{ij} \left(\frac{\tau_u}{m} \right) \right) \right\} \tag{17}$$

(2) Elements of matrix \mathbf{R}_{Nd} :

$$[\mathbf{R}_1]_i = -m\alpha_i \sum_{u=0}^Z \left\{ \left(\sum_{v=-p}^{-1} G(t_{u+1,v}, t_{u+1,v+1})\kappa_v + \sum_{v=1}^{N-p} G(t_{u+1,v-1}, t_{u+1,v})\kappa_v \right) \left(E_{ij} \left(\frac{\tau_{u+1}}{m} \right) - E_{ij} \left(\frac{\tau_u}{m} \right) \right) + \left[\sum_{v=-p}^{-1} G(t_{u+1,v}, t_{u+1,v+1})c_v + \sum_{v=1}^{N-p} G(t_{u+1,v-1}, t_{u+1,v})c_v \right] \sum_{j=0}^{mH} \alpha_j \omega_0 \left[-a_j \left(B_{ij} \left(\frac{\tau_{u+1}}{m} \right) - B_{ij} \left(\frac{\tau_u}{m} \right) \right) + b_j \left(A_{ij} \left(\frac{\tau_{u+1}}{m} \right) - A_{ij} \left(\frac{\tau_u}{m} \right) \right) \right] \right\} \tag{18}$$

$$[\mathbf{R}_2]_i = -m \sum_{u=0}^Z \left\{ \left(\sum_{v=-p}^{-1} G(t_{u+1,v}, t_{u+1,v+1})\kappa_v + \sum_{v=1}^{N-p} G(t_{u+1,v-1}, t_{u+1,v})\kappa_v \right) \left(F_{ij} \left(\frac{\tau_{u+1}}{m} \right) - F_{ij} \left(\frac{\tau_u}{m} \right) \right) + \left[\sum_{v=-p}^{-1} G(t_{u+1,v}, t_{u+1,v+1})c_v + \sum_{v=1}^{N-p} G(t_{u+1,v-1}, t_{u+1,v})c_v \right] \sum_{j=0}^{mH} \alpha_j \omega_0 \left[-a_j \left(D_{ij} \left(\frac{\tau_{u+1}}{m} \right) - D_{ij} \left(\frac{\tau_u}{m} \right) \right) + b_j \left(C_{ij} \left(\frac{\tau_{u+1}}{m} \right) - C_{ij} \left(\frac{\tau_u}{m} \right) \right) \right] \right\} \tag{19}$$

where

$$\begin{aligned} \kappa_{-i} &= \sum_{j=2}^i (c_{-j+1} - c_{-j})d_{-j+1}, \\ \kappa_i &= \sum_{j=2}^i (c_{j-1} - c_j)d_{j-1}, \quad i > 0 \\ \alpha_i &= \begin{cases} 1, & i \neq 0 \\ 0.5 & i = 0 \end{cases} \end{aligned} \tag{20}$$

(3) Matrix \mathbf{S}_{Nd} can be got by multiplying matrix \mathbf{C}_{Nd} and determinant \mathbf{A} .

The expressions of $A_{ij}(\tau)$, $B_{ij}(\tau)$, $C_{ij}(\tau)$, $D_{ij}(\tau)$, $E_{ij}(\tau)$, $F_{ij}(\tau)$ can be referred to Lau [34].

3.2 Hysteretic model treatment

In the hysteretic model, the process shows the differences compared with the above nonlinear damping systems, which consist of only velocity items. When the loading/unloading state is determined, the nonlinear force degenerates to the nonlinear stiffness characteristics. Therefore, another step function is

added to determine the state of the current motion, which can be defined below:

$$G(\dot{y}_0) = \begin{cases} 1, & \dot{y}_0 \geq 0 \\ 0, & \text{elsewise} \end{cases} \tag{21}$$

$G(\dot{y}_0)$ can be utilized in the equivalent piecewise-linearization process. For example, in the interval $[y_i, y_{i+1}]$, assuming that the stiffness for the loading state and unloading state are k_u and k_l , respectively. The equivalent stiffness k_{eq} can be written as:

$$k_{eq} = (k_u - k_l)G(\dot{y}_0) + k_l \tag{22}$$

Once the above equivalent stiffness is obtained, a similar procedure can be adopted to solve the vibrational characteristics of the hysteretic nonlinearities.

First, the displacement restoring force under the loading/unloading state is divided by the discrete node process with the same node division method, and the displacement nodes y_i ($i = -p, \dots, N - p$) of both states remain the same. The linearized error ε is checked to ensure that the maximum results error is within the allowable range. Second, all roots of τ for $y - y_i = 0$ and $dy/d\tau = 0$ are computed, and then arranged in ascending order. Third, step functions are used to define the loading/unloading state for every adjacent minimum interval. And the equivalent stiffness stiffnesses are obtained for the piecewise-linear IHBM to solve Eq. (11).

3.3 Stability of the periodic solution

Using Floquet theory, the perturbation of the solution is investigated. Assume the small turbulence solution at the ω_0 state of y_0 for Eq. (11) is defined by δy , and the solution after perturbation can be expressed by

$$y = y_0 + \delta y \tag{23}$$

Equation (23) is substitute into Eq. (11), and Eq. (11) still holds for the original state with y_0 . The linearized equation for small perturbation δy can be obtained as follows:

$$\omega_0^2 \delta \ddot{y} + 2\xi \omega_0 \delta \dot{y} + \frac{g(\dot{y}_0 + \delta \dot{y}) - g(\dot{y}_0)}{\delta \dot{y}} + \frac{q(y_0 + \delta y) - q(y_0)}{\delta y} = 0 \tag{24}$$

By the definition of $g(\dot{y})$ and $q(y)$, the last two terms of Eq. (24) on the left-hand side can be written using step functions:

$$C_{nl} = \frac{g(\dot{y}_0 + \delta \dot{y}) - g(\dot{y}_0)}{\delta \dot{y}} = \sum_{v=-p}^{-1} G(t_{u+1,v}, t_{u+1,v+1})c_v + \sum_{v=1}^{N-p} G(t_{u+1,v-1}, t_{u+1,v})c_v \tag{25}$$

$$K_{nl} = \frac{q(y_0 + \delta y) - q(y_0)}{\delta y} = \sum_{v=-q}^{-1} G(s_{u+1,v}, s_{u+1,v+1})k_v + \sum_{v=1}^{M-q} G(s_{u+1,v-1}, s_{u+1,v})k_v \tag{26}$$

In Eq. (26), $s_{1,n}, s_{2,n}, \dots, s_{M+1,n}$ are the sign functions of $y_0 - e_n$ ($n = -p_k - 1, -p_k, \dots, -1, 0, 1, \dots, M - p_k + 1$), and k_n and e_n ($n = -p_k - 1, -p_k, \dots, -1, 0, 1, \dots, M - p_k + 1$) are the stiffnesses and displacements, respectively, for the nonlinear stiffness systems. The symbols p_k and M for the nonlinear stiffness are similar to the description in Fig. 1 and Eq. (2). Equation (24) can be transformed into the linear ordinary differential equation:

$$\dot{\mathbf{Y}} = \mathbf{Q}(\tau)\mathbf{Y} \tag{27}$$

where

$$\mathbf{Y} = [\delta y, \delta \dot{y}]^T$$

$$\mathbf{Q}(\tau) = \begin{bmatrix} 0 & 1 \\ -\frac{K_{nl}}{\omega_0^2} & -\frac{2\xi + C_{nl}}{\omega_0} \end{bmatrix} \tag{28}$$

The standard process for Floquet theory can be adopted by obtaining the monodromy matrix \mathbf{P} from the matrix $\mathbf{Q}(\tau)$ which can be referred to Wang [6]. The Floquet multipliers, which are calculated by the eigenvalues of the monodromy matrix \mathbf{P} , are acquired to decide the stability of the solutions, and the judgment condition is whether any eigenvalue leaves the unit circle. The acquisition of the monodromy matrix \mathbf{P} can be proceeded in Eq. (30) by assuming that matrix $\mathbf{Q}(\tau)$ is constant between τ_{m-1} and τ_m with a relatively small interval length of $\Delta_m = \tau_m - \tau_{m-1}$:

$$\mathbf{M}_m = \frac{1}{\Delta_m} \int_{\tau_{m-1}}^{\tau_m} \mathbf{Q}(\tau) d\tau \tag{29}$$

$$\mathbf{P} = \prod_{i=1}^{N_m} \exp(\Delta_m \mathbf{M}_m) \tag{30}$$

where period $2m\pi$ is divided into N_m intervals for stability analysis.

4 Numerical applications

In this section, eight nonlinear damping systems are investigated by the proposed method. First, a typical polynomial damping system is analyzed to show the relationship of the discrete number, linearized error and result error. Second, hysteretic models, including the bilinear model and Bouc–Wen models, are adopted. Third, nonlinear SDOF systems that

compromises of both nonlinear stiffness and damping are investigated. Last, this method is extended to MDOF systems.

4.1 Validations

An example of the nonlinear damping SDOF system with unstable solutions can be described in Eq. (31). Habib [9] investigated a harmonically excited, SDOF oscillator with isolated resonance curves (IRC):

$$\ddot{y} + y + c_1\dot{y} + c_3y^3 + y^5 = 2f \cos(\omega t) \tag{31}$$

The nonlinear part of this oscillator is a polynomial damping, which is solved by the averaging method [9]. Figure 3 shows the characteristics of the nonlinear damping with the velocity region from -1.2 to 1.2 . The plot shows that when $-0.7 < y < 0.7$, $h(y)$ frustrates slightly, and the curvature is small.

Due to the complexity of the nonlinear damping, unstable solutions can be obtained within the frequency range from 0.8 to 1.2 for the case $f = 0.01$, $c_1 = 0.1$, and $c_3 = -0.6$. This can be found from Fig. 4, where there are two regions, namely $[0.985, 0.991]$ and $[1.009, 1.015]$, and the Floquet multipliers are larger than 1. This finding is consistent with the results computed by Habib. The result obtained by the improved DIHBM and by the numerical simulation, such as the Runge–Kutta method (RKM), are almost

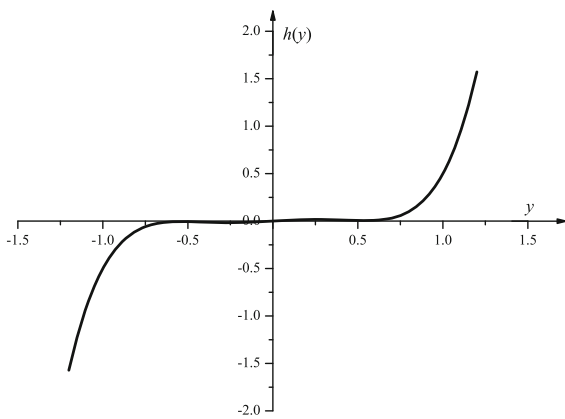


Fig. 3 Damping curves of the nonlinear model

Fig. 4 Response diagram for $f = 0.01$: **a** frequency response curve of the amplitude, the solid line refers to the results of $N = 50$, the hollow circle denotes the results of MatCont; and the triangle is obtained by Habib [9]; **b** eigenvalues of the monodromy matrix \mathbf{P} compared with ω

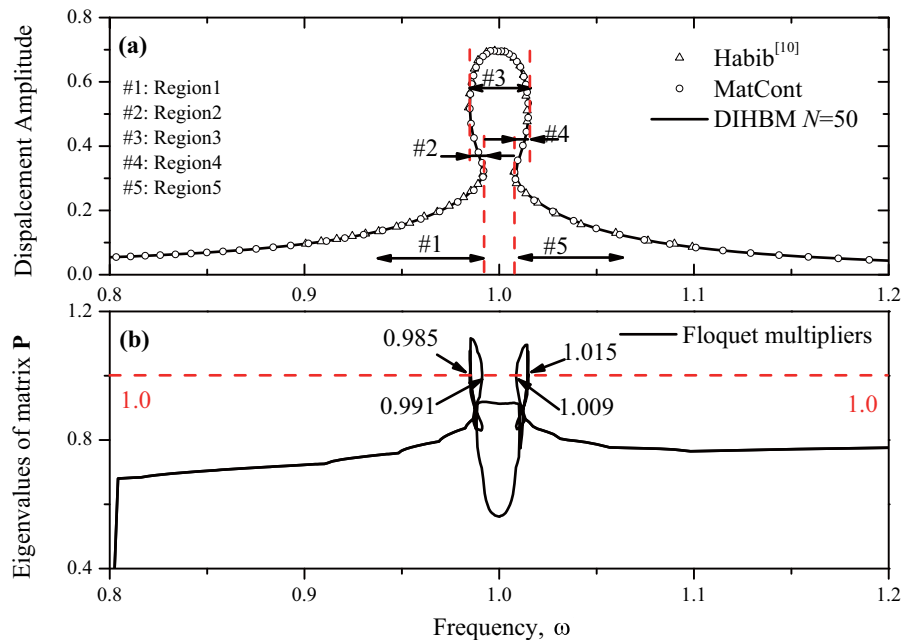


Fig. 5 Frequency response curves of the polynomial damping system for different N

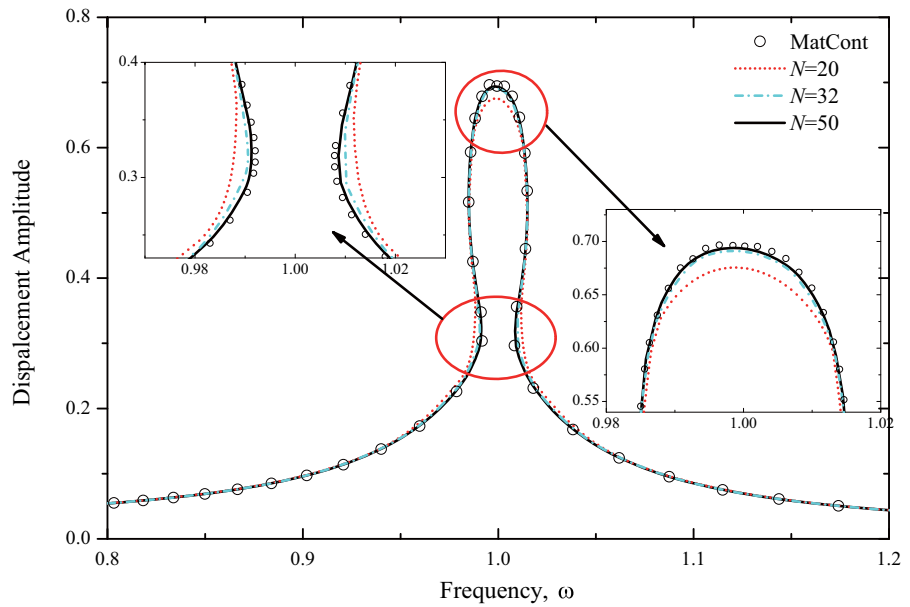
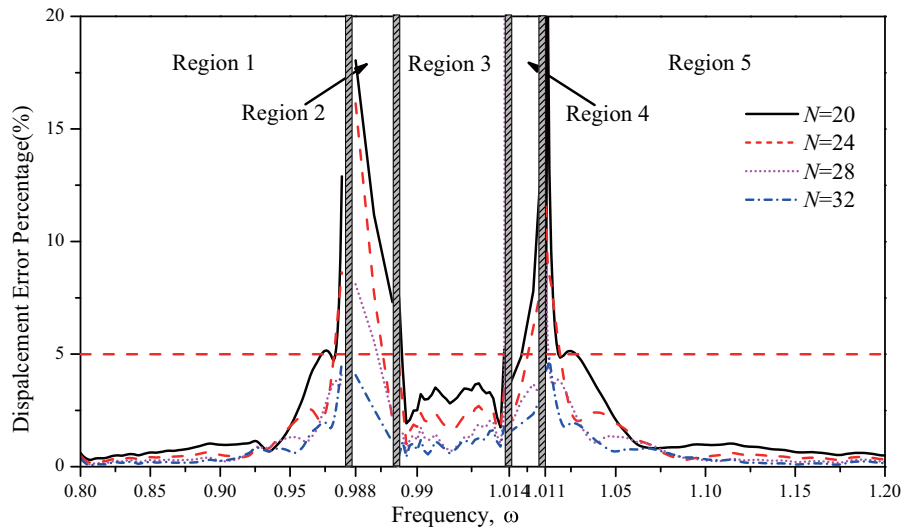


Fig. 6 The result errors of the polynomial damping system for different N



equivalent. As the unstable regions cannot be obtained from RKM, the reference result for the calibration is chosen from the result by the numerical continuation and bifurcation tool MatCont [35].

Figure 5 illustrates the effects of different N values from 20 to 50 on the frequency response curves of this polynomial damping system. The results are compared with the reference result obtained by the MatCont. Major result errors occur in the turning unstable regions and the maximum resonance region.

As shown in Fig. 4a, there are five regions divided by two unstable parts. Figure 6 calculates the result errors of different discrete numbers for the five regions. The maximum result errors are located at the transitions between the stable region and unstable region. The result errors decrease with an increase in N . The traditional IHBM can be regarded as the DIHBM with the discrete number approaching to infinity. To balance the computational speed and accuracy, a proper discrete number is essential to choose within an allowable error value in advance, for

example, 5% in this paper. When N is increased to 32, the maximum result error decreases to 4.82%, which is less than the predetermined result error.

This calibration is assumed to extend to the nonlinear damping systems, and the approximate linearized error of 1.4×10^{-3} can meet the requirement of the allowable error for engineering applications. In addition, if the order of the polynomial damping curve is relatively high or the nonlinear damping curve is nonsmooth, the discrete number should be set to a larger value or refinements of these regions are needed. Otherwise, the discrete number can be selected to a much smaller value.

4.2 Numerical investigation of the hysteretic models

4.2.1 Bilinear hysteretic model

In Sect. 2.2, the characteristics of the bilinear hysteretic model are introduced. A bilinear model is shown in Fig. 7. The loading/unloading displacement regime falls between -0.15 and 0.15 . The nonlinear restoring force can be expressed by six linear functions, namely Regimes I ~ VI. If the maximum displacement is less than 0.15 , Regimes I and VI are omitted, and the displacements of points B and D are dependent on the response of the system.

$$F(y, \dot{y}) = \begin{cases} 10y + 1.1, & \text{Regime I} \\ 10y + 1.1, & \text{Regime II} (\dot{y} > 0) \\ 1.2y + 0.22, & \text{Regime III} (\dot{y} > 0) \\ 10y - 1.1, & \text{Regime IV} (\dot{y} \leq 0) \\ 10y - 1.1, & \text{Regime V} (\dot{y} \leq 0) \\ 1.2y - 0.22, & \text{Regime VI} \end{cases} \quad (32)$$

Generally, the above functions are not essential to the proposed method. Only six points, namely, A ~ F, which can depict the whole loading/unloading procedure (including the velocity item of y), are needed to compute the dynamics of the system.

The nondimensional governing equation is described below:

$$\ddot{y} + 2\xi\dot{y} + F(y, \dot{y}) = f \cos(\omega t) \quad (33)$$

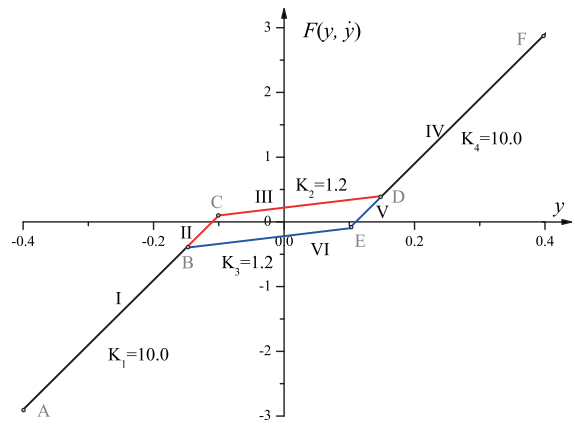


Fig. 7 Stiffness-damping characteristic curve of bilinear hysteretic model

where $\zeta = 0.05$ and $f = 1.0$. The number of harmonics is set to 3 to cover all the fundamental frequency responses. Figure 8 presents the frequency response curves of the bilinear hysteretic system. The results from the proposed DIHBM match those obtained by the RKM and Computational Continuation Core (COCO) [36], which is available for nonsmooth nonlinear dynamical problems.

The stiffness ratio is 8.33 in adjacent intervals near points B and D for both the loading state and unloading state, which implies that this hysteretic model may show strong nonlinearity and that the proposed method can provide a systematic procedure to acquire the dynamics of the system. When the frequency ranges from 3.112 to 2.903, the unstable region occurs as the Floquet multipliers leave the unit circle.

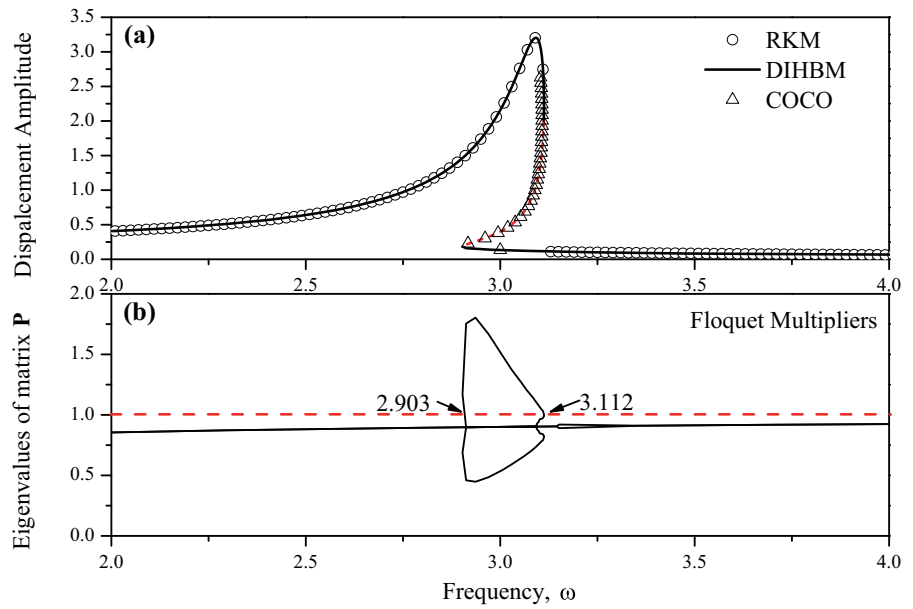
4.2.2 Bouc–Wen model

The bilinear model can be regarded as the special case of the Bouc–Wen model for the proposed method. However, the linearized error occurs when the system is shifted from the Bouc–Wen model to the piecewise-linear hysteretic model.

The dynamical equations for the Bouc–Wen model can be expressed by:

$$\begin{aligned} \ddot{y} + 2\xi\omega_0\dot{y} + v\omega_0^2y + (1 - \gamma)\omega_0^2z &= B \sin(\omega t) \\ \dot{z} &= Ay - \alpha|y|z|z|^{n-1} - \beta\dot{y}|z|^n \end{aligned} \quad (34)$$

Fig. 8 Response diagram for the bilinear hysteretic model: **a** frequency response curve of the amplitude; **b** the eigenvalues of the monodromy matrix **P** compared with ω



The parameters A , α , β , and n are non-dimensional Bouc–Wen parameters fitted by experimental data of the hysteretic force z . In this paper, n is set to 1 to obtain the explicit expressions of the Bouc–Wen model, and the hysteresis loop can be expressed by four parts on the displacement \times force plane considering the signs of \dot{y} and z [37]. The expressions are

$$z_I = \begin{cases} \frac{A}{\alpha - \beta} \left(1 - e^{-(\alpha - \beta)(y - y_0)} \right), & \alpha \neq \beta \\ A(y - y_0), & \alpha = \beta \end{cases}, \text{Regime I} \\ : \dot{y} \leq 0, z > 0 \tag{35}$$

$$z_{II} = \begin{cases} -\frac{A}{\alpha + \beta} \left(1 - e^{(\alpha + \beta)(y - y_0)} \right), & \alpha \neq -\beta \\ A(y - y_0), & \alpha = -\beta \end{cases}, \text{Regime II} \\ : \dot{y} \leq 0, z \leq 0 \tag{36}$$

$$z_{III} = \begin{cases} -\frac{A}{\alpha - \beta} \left(1 - e^{(\alpha - \beta)(y + y_0)} \right), & \alpha \neq \beta \\ A(y + y_0), & \alpha = \beta \end{cases}, \text{Regime III} \\ : \dot{y} > 0, z \leq 0 \tag{37}$$

$$z_{IV} = \begin{cases} \frac{A}{\alpha + \beta} \left(1 - e^{-(\alpha + \beta)(y + y_0)} \right), & \alpha \neq -\beta \\ A(y + y_0), & \alpha = -\beta \end{cases}, \text{Regime IV} \\ : \dot{y} > 0, z > 0 \tag{38}$$

In the above equations, y_0 is the displacement at $z = 0$ and can be obtained by the experiment in advance or by the displacement responses. In the latter situation, another Newton-Rapson iteration, whose computations are more time-consuming, is needed, as the displacement integral constant is the variable that needs to be solved in the proposed method.

In this section, two typical Bouc–Wen cases, namely (a) $\alpha = 0.1$, $\beta = 0.5$; (b) $\alpha = 0.1$, $\beta = -0.5$, are investigated by the proposed method. Other parameters shown in Eq. (34) are $\zeta = 0.05$, $n = 1$, $v = 0.05$, $\omega_0 = 1.0$, $\gamma = 0$, $A = 0.95$, $B = 0.5$ which are equivalent to those of Okuizumi [38], the results are compared with the multiple time scale method. Figure 9 depicts the restoring forces with displacements.

The number of harmonics is set to 3 to satisfy the computational accuracy. There are eight regimes for the discrete node process, and each regime is uniformly divided. Note that Regimes 1 and 8, Regimes 2 and 7, Regimes 3 and 6, Regimes 4 and 5 use the same

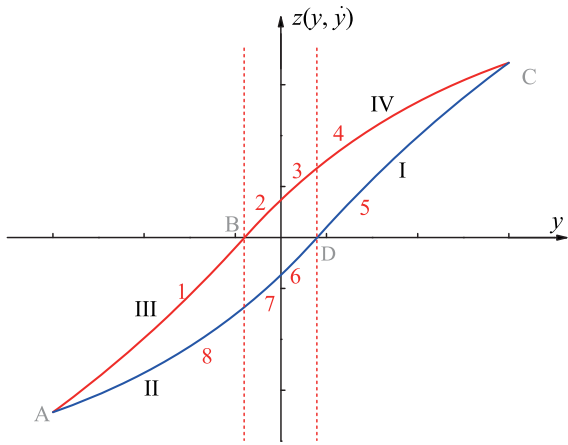


Fig. 9 Restoring force characteristics of the Bouc–Wen model

division method (the division strategy for Case b is similar to Case a). The discrete numbers and linearized errors for the situation, where the maximum displacement is set to 2.0 as an example, are listed in Table 1. The linearized errors for both cases are less than 1.4×10^{-3} , which can meet the allowed error limit.

Figure 10 shows that the results computed by the proposed method and multiple time scale (MTS) method are consistent with those by the COCO. The hollow circle represents the numerical results by the COCO, the hollow triangle illustrates the results by Okuizumi [38], and the black solid line denotes the solutions obtained by the proposed method. From the plots, the proposed method is more accurate than the MTS method including the unstable regions in

Table 1 Relationship between the discrete number and the linearized error for both cases

Case a				Case b			
Regime	Displacement range	Discrete number, N	Linearized error	Regime	Displacement range	Discrete number, N	Linearized error
1	$[- 3.8 - 1]$	4	4.6×10^{-4}	1	$[- 3.8 - 1]$	5	4.1×10^{-4}
2	$[- 1 - 0.16]$	2	4.0×10^{-4}	2	$[- 1 - 0.37]$	1	1.0×10^{-3}
3	$[- 0.16 0]$	3	0.3×10^{-4}	3	$[- 0.37 0]$	3	1.5×10^{-4}
4	$[0 0.16]$	3	0.3×10^{-4}	4	$[0 0.37]$	3	1.1×10^{-4}
5	$[0.16 1]$	2	1.5×10^{-3}	5	$[0.37 1]$	1	1.6×10^{-3}
6	$[1 3.8]$	4	4.6×10^{-4}	6	$[1 3.8]$	5	4.1×10^{-4}
7	$[0.16 1]$	–	4.0×10^{-4}	7	$[0.37 1]$	–	1.0×10^{-3}
8	$[0 0.16]$	–	0.3×10^{-4}	8	$[0 0.37]$	–	1.5×10^{-4}
9	$[- 0.16 0]$	–	0.3×10^{-4}	9	$[- 0.37 0]$	–	1.1×10^{-4}
10	$[- 1 - 0.16]$	–	1.5×10^{-3}	10	$[- 1 - 0.37]$	–	1.6×10^{-3}
Total	$[- 3.8 3.8]$	18	6.7×10^{-4}	Total	$[- 3.8 3.8]$	18	6.9×10^{-4}

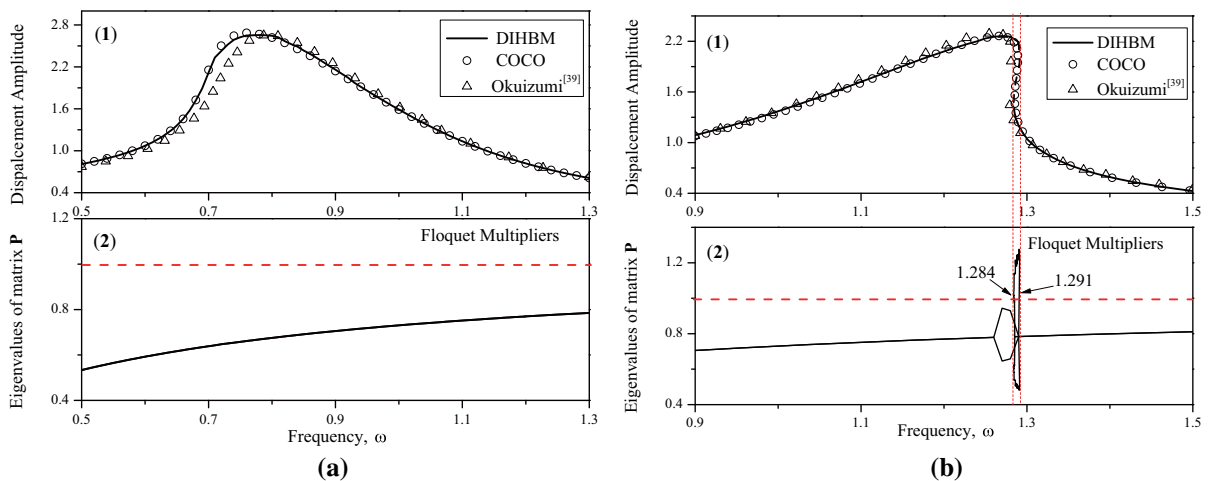


Fig. 10 Response diagram for the Bouc–Wen model of case a ($\alpha = 0.1$ and $\beta = 0.5$) and case b ($\alpha = 0.1$ and $\beta = -0.5$): **1** frequency response curve of the amplitude; **2** eigenvalues of the monodromy matrix \mathbf{P} compared with ω

Fig. 10b. The softening characteristics are revealed as the peak frequency shifts to the left in Case a, and the hardening features are represented as it shifts to the right in Case b.

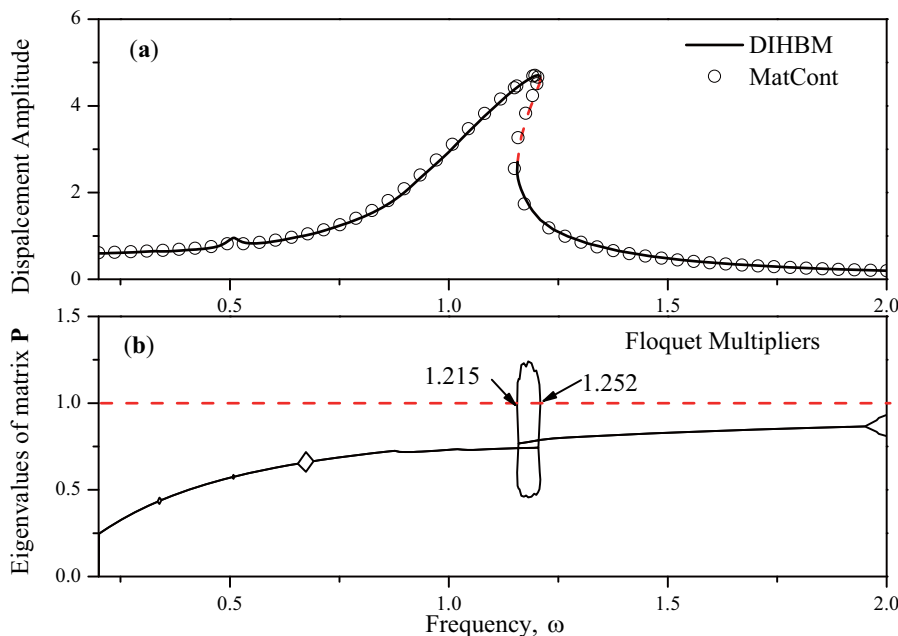
4.3 Numerical investigation of the complex models

Apart from nonlinear damping, the improved method can obtain period solutions of most continuous types of nonlinear systems. Gao [5] investigated a compact quasi-zero frequency vibration isolator (VI) with a high-static and low-dynamic stiffness (HSLD) and fluid damping device. The dynamics of this new device can be solved by the proposed method, while the averaging method would cause computational errors under strong nonlinearity. In addition, the experimental data of the stiffness characteristics can be directly applied to the proposed method without adopting the curve fitting techniques.

The control equation obtained by Gao is given in Eq. (39), where the second, third and fourth terms on the left side of the equation denote the HSLD stiffness fitted by the experimental results, and the fifth and sixth terms represent the nonlinear fluid damping, which is obtained by the empirical data.

$$\ddot{y} + \omega_0^2 y + \alpha_2 y^2 + \alpha_3 y^3 + c_1 \dot{y} + c_2 y |\dot{y}| = F_1 \cos \omega t \tag{39}$$

Fig. 11 Response diagram for the SDOF complex model: **a** frequency response curve of the amplitude; **b** eigenvalues of the monodromy matrix **P** compared with ω



Transforming Eq. (39), the nondimensional equation can be acquired:

$$\ddot{z} + z + k_2 z^2 + k_3 z^3 + d_1 \dot{z} + d_2 z |\dot{z}| = f \cos(\tau) \tag{40}$$

where

$$y = Az, d_1 = \frac{c_1}{\omega_0}, d_2 = c_2 A, k_2 = \frac{\alpha_2 A}{\omega_0^2}, k_3 = \frac{\alpha_3 A^2}{\omega_0^2} f = \frac{F}{A \omega_0^2} \tag{41}$$

The parameters are listed as follows: $A = 0.001$ m, $d_1 = 0.0815$, $d_2 = 0.005$, $k_2 = 0.085$, $k_3 = 0.03$, and $f = 0.59$. The discrete number for the fluid damping is 10; the corresponding linearized error is 1.04×10^{-5} ; and N for the nonlinear stiffness is 14 with a linearized error of 5.81×10^{-4} .

Unlike the traditional averaging method, which is inaccurate in the peak resonance region and is hard to show subharmonic resonance, the proposed method can give detailed information with high accuracy in Fig. 11. Additionally, the unstable zone calculated by the eigenvalues is suitable for the design criterion in jump avoidance.

Carpineto [39] introduced a hysteretic damper into the passive nonlinear TMD and discovered that reasonable selection of parameters, especially the excitation amplitude, would enable a system transition from softening to hardening. The control equation is described below:

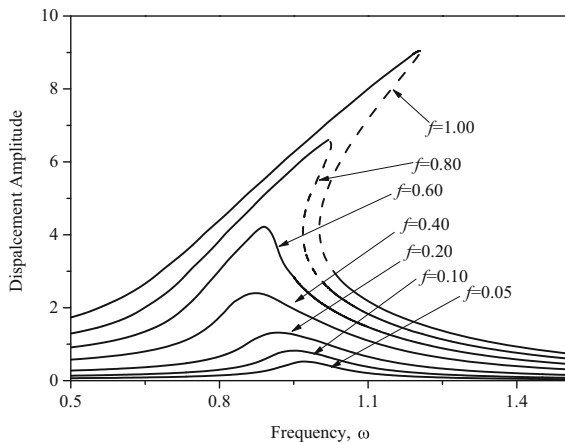


Fig. 12 Frequency–response curves of the softening-hardening TMD with different excitation amplitudes; the dashed line denotes unstable solutions

$$\ddot{y} + 2\zeta\dot{y} + ky + k_3y^3 + z = f \cos(\tau) \tag{42}$$

$$z = (1 - k)y - \alpha|y|z|z|^{n-1} - \beta|y|z|^n$$

The softening Bouc–Wen model ($\alpha + \beta > 0$) is applied in this softening-hardening TMD. Figure 12 shows the frequency–response curves of the TMD with different excitation amplitudes by the proposed method; the other parameters are $\zeta = 0.022$, $n = 1$, $k = 0.52$, $k_3 = 0.015$, $\alpha = 0.5$, and $\beta = 0.5$. When f is small, the material nonlinearity dominates the frequency response curve. As f gradually increases, the frequency response curve gradually changes from a softening characteristic to a hardening characteristic, indicating that the geometrical nonlinearity has a major role in the frequency response curve.

4.4 Numerical investigation of the MDOF nonlinear system

In engineering applications, the MDOF system is introduced and designed in certain vibration isolators/absorbers or energy harvester for better performance. The proposed method can be an alternative way to solve the dynamics of these systems. Assuming that a N_D DOF system without coupling of degrees of freedom, and that the coupling of displacement and

velocity for each degree of freedom is limited to hysteresis, the force for each DOF can be expressed by:

$$f_j = \sum_{i=1}^{N_1} r_{ji}(y_i) + \sum_{i=1}^{N_2} h_{ji}(\dot{y}_i) + \sum_{i=1}^{N_3} z_{ji}(y_i, \dot{y}_i), j = 1, 2, \dots, N_D \tag{43}$$

where the symbols r , h , and z refer to the force of nonlinear stiffness, nonlinear damping and hysteresis, respectively. N_1 , N_2 and N_3 are the numbers of the nonlinear terms of the above forces. After satisfying the linearized error condition, Eq. (43) can be written by the piecewise-linear form for each DOF:

$$f_j \approx \sum_{i=1}^{N_1} q_{ji}(y_i) + \sum_{i=1}^{N_2} g_{ji}(\dot{y}_i) + \sum_{i=1}^{N_3} zd_{ji}(y_i, \dot{y}_i), j = 1, 2, \dots, N_D \tag{44}$$

where symbols q , g , and zd refer to the force of piecewise-linear stiffness, damping and hysteresis, respectively. The dynamic equations can be written in matrix form:

$$M \frac{d^2 \mathbf{y}}{dt^2} + C \frac{d\mathbf{y}}{dt} + K\mathbf{y} + \begin{bmatrix} \sum_{i=1}^{N_1} q_{1i}(y_i) + \sum_{i=1}^{N_2} g_{1i}(\dot{y}_i) + \sum_{i=1}^{N_3} zd_{1i}(y_i, \dot{y}_i) \\ \dots \\ \sum_{i=1}^{N_1} q_{N_D i}(y_i) + \sum_{i=1}^{N_2} g_{N_D i}(\dot{y}_i) + \sum_{i=1}^{N_3} zd_{N_D i}(y_i, \dot{y}_i) \end{bmatrix} = \mathbf{e}(\tau) \tag{45}$$

The nonlinear matrices C_{NK} , C_{ND} , R_{NK} , R_{ND} for each nonlinear DOF can be calculated by Eqs. (14)–(19). Equation (4) can be extended to Eq. (43) by the expansion of the matrix dimension in the DIHBM. Noting that each DOF is independent according to the assumption, Eq. (45) can be solved directly using the procedure in Sect. 3.

Zhang [40] analyzed 1-DOF and 2-DOF nonlinear energy sink (NES) with geometrically nonlinear damping and stiffness. A schematic diagram of a linear oscillator with 1-DOF NES is depicted in Fig. 13a. The nonlinear stiffness of the NES is composed of the linear stiffness k_{221} and nonlinear cubic stiffness k_{223} , the damping part is a nonlinear cubic damping with damping coefficient λ . An

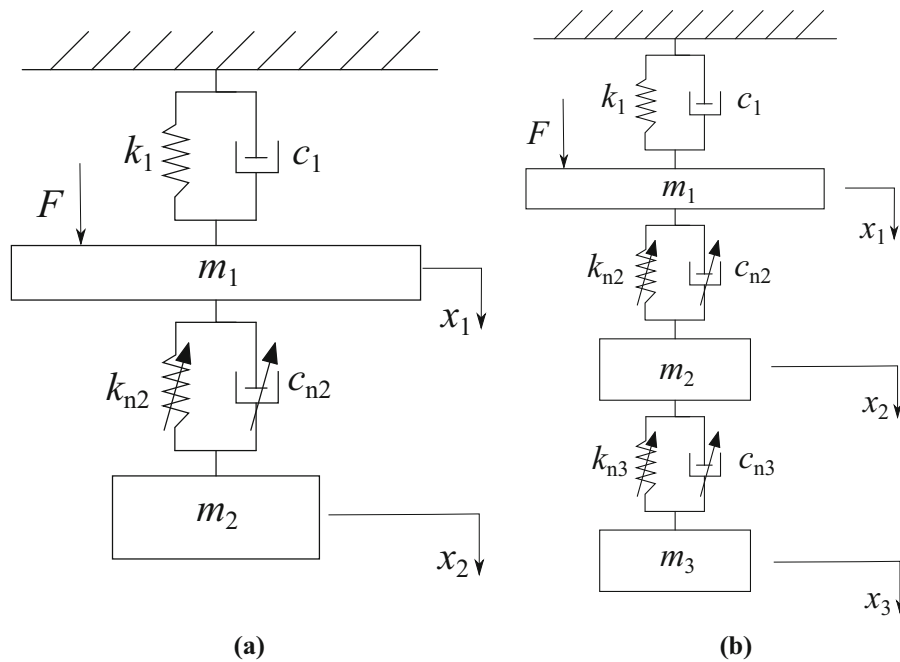


Fig. 13 Schematic of a linear oscillator with 1-DOF NES and 2-DOF NES

external harmonic force is applied to m_1 with amplitude A . The mathematical model of this NES is derived below:

$$\begin{aligned} \ddot{x}_1 + x_1 + \varepsilon k_{221}(x_1 - x_2) + \varepsilon k_{223}(x_1 - x_2)^3 \\ + \varepsilon \lambda (\dot{x}_1 - \dot{x}_2)^3 = \varepsilon A \cos(\omega t) \\ \ddot{x}_2 - k_{221}(x_1 - x_2) - k_{223}(x_1 - x_2)^3 \\ - \lambda (\dot{x}_1 - \dot{x}_2)^3 = 0 \end{aligned} \tag{46}$$

where ε is the mass ratio of m_2 and m_1 . The linear damping c_1 is disregarded in this case. Setting $y_1 = x_1 - x_2$ and $y_2 = x_2$, Eq. (46) can be rewritten in matrix form:

$$\begin{bmatrix} \frac{1}{\varepsilon} & \frac{1}{\varepsilon} \\ \frac{\varepsilon}{0} & \frac{\varepsilon}{1} \end{bmatrix} \begin{bmatrix} \ddot{y}_1 \\ \ddot{y}_2 \end{bmatrix} + \begin{bmatrix} \frac{1}{\varepsilon} + k_{221} & \frac{1}{\varepsilon} \\ -k_{221} & 0 \end{bmatrix} \begin{bmatrix} y_1 \\ y_2 \end{bmatrix} + \mathbf{F}_{nl} + \mathbf{H}_{nl} = \begin{bmatrix} A \cos(\omega t) \\ 0 \end{bmatrix} \tag{47}$$

where \mathbf{F}_{nl} and \mathbf{H}_{nl} are defined as listed below and can be linearized by \mathbf{G}_{stiff} and \mathbf{G}_{damp} , respectively, using the discrete node process. The parameters are $\lambda = 0.3$, $\varepsilon = 0.1$, $k_{221} = 1.333$, $k_{223} = 0.333$ and $A = 0.3$.

$$\mathbf{F}_{nl} = \begin{bmatrix} k_{223}y_1^3 \\ -k_{223}y_1^3 \end{bmatrix}, \mathbf{H}_{nl} = \begin{bmatrix} \lambda y_1^3 \\ -\lambda y_1^3 \end{bmatrix} \tag{48}$$

The discrete number for the nonlinear item on \mathbf{G}_{stiff} is 16 for the interval from -1.5 to 1.5 ; the linearized error is 1.2×10^{-3} ; and this value for the nonlinear item on \mathbf{G}_{damp} is 26 in the region from -3 to 3 , where the linearized error is decreased to 1.2×10^{-3} .

Figure 14 illustrates the response characteristics of the linear oscillator with 1-DOF NES. The amplitudes of y_1 and y_2 obtained by the proposed method show agreement with those obtained by the numerical simulation of MatCont.

Furthermore, the linear oscillator with 2-DOF NES is solved by the DIHBM. Shown in Fig. 13b, the nondimensional mathematical model of this NES is expressed as follows:

$$\begin{aligned} \ddot{x}_1 + 2\xi\dot{x}_1 + x_1 + \varepsilon k_{221}(x_1 - x_2) + \varepsilon k_{223}(x_1 - x_2)^3 \\ + \varepsilon \lambda_1 (\dot{x}_1 - \dot{x}_2)^3 = \varepsilon A \cos(\omega t) \\ \eta \ddot{x}_2 - k_{221}(x_1 - x_2) - k_{223}(x_1 - x_2)^3 - \lambda_1 (\dot{x}_1 - \dot{x}_2)^3 \\ + k_{331}(x_2 - x_3) + k_{333}(x_2 - x_3)^3 + \lambda_2 (\dot{x}_2 - \dot{x}_3)^3 = 0 \\ (1 - \eta) \ddot{x}_3 - k_{331}(x_2 - x_3) - k_{333}(x_2 - x_3)^3 - \lambda_2 (\dot{x}_2 - \dot{x}_3)^3 = 0 \end{aligned} \tag{49}$$

where $\varepsilon\eta$ and $\varepsilon(1-\eta)$ are the mass ratios of m_2/m_1 and m_3/m_1 , respectively. Setting $y_1 = x_1 - x_2$, $y_2 = x_2 - x_3$, and $y_3 = x_3$, Eq. (49) can be arranged in matrix form:

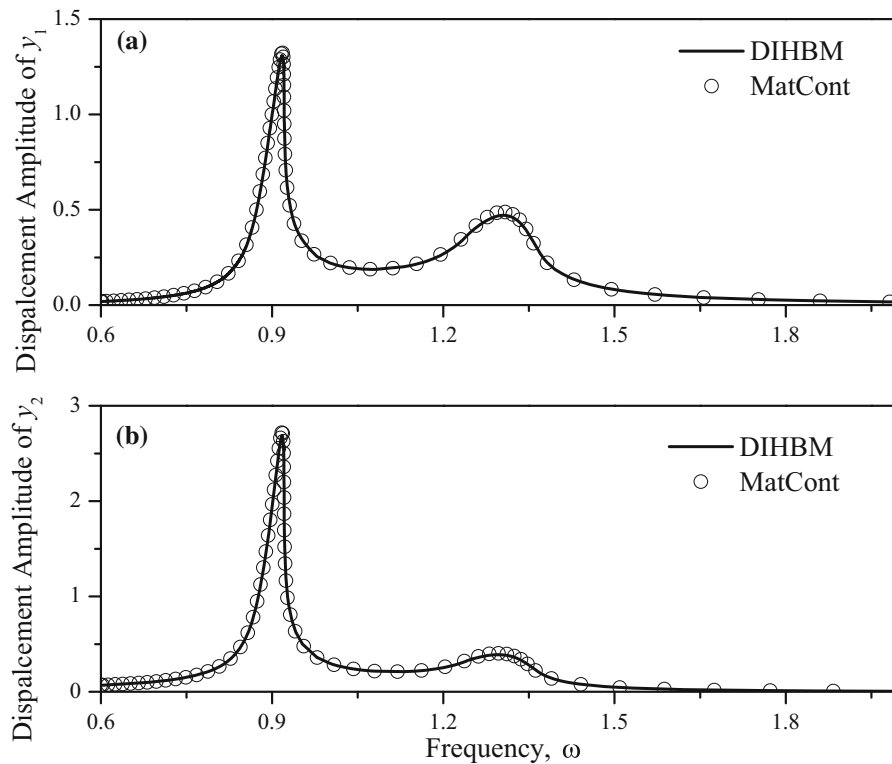


Fig. 14 Response diagram for a linear oscillator with 1-DOF NES: **a** frequency response curve of amplitude of y_1 ; **b** frequency response curve of amplitude of y_2

$$\begin{aligned}
 & \begin{bmatrix} 11 & 1 \\ \varepsilon & \varepsilon & \varepsilon \\ 0 & \eta & \eta \\ 00 & 1 - \eta \end{bmatrix} \begin{bmatrix} \ddot{y}_1 \\ \ddot{y}_2 \\ \ddot{y}_3 \end{bmatrix} + \begin{bmatrix} 2\xi & 2\xi & 2\xi \\ \varepsilon & \varepsilon & \varepsilon \\ 0 & 0 & 0 \\ 0 & 0 & 0 \end{bmatrix} \begin{bmatrix} \dot{y}_1 \\ \dot{y}_2 \\ \dot{y}_3 \end{bmatrix} \\
 & + \begin{bmatrix} k_{221} + \frac{1}{\varepsilon} & \frac{1}{\varepsilon} & \frac{1}{\varepsilon} \\ -k_{221} & k_{331} & 0 \\ 0 & -k_{331} & 0 \end{bmatrix} \begin{bmatrix} y_1 \\ y_2 \\ y_3 \end{bmatrix} \\
 & + \begin{bmatrix} k_{223}y_1^3 \\ -k_{223}y_1^3 + k_{333}y_2^3 \\ -k_{333}y_2^3 \end{bmatrix} + \begin{bmatrix} \lambda_1 y_1^3 \\ -\lambda_1 y_1^3 + \lambda_2 y_2^3 \\ -\lambda_2 y_2^3 \end{bmatrix} = \begin{bmatrix} A \cos(\omega t) \\ 0 \\ 0 \end{bmatrix} \tag{50}
 \end{aligned}$$

The parameters are $\varepsilon = 0.1$, $\eta = 0.6$, $\xi = 0.02$, $\lambda_1 = 0.3$, $\lambda_2 = 0.3$, $k_{221} = 0.133$, $k_{223} = 1.333$, $k_{331} = 0.133$, $k_{333} = 1.333$ and $A = 0.3$. The dividing method for the discrete node process is similar to the 1-DOF NES case.

Figure 15 shows the frequency response curves of each DOF. Comparison with the results from MatCont verifies the accuracy of the proposed DIHBM

including the two unstable regimes $[0.403, 0.670]$ and $[1.109, 1.120]$.

Moreover, the hysteretic model can be adopted in the MDOF system. The nonlinear cubic item k_{n2} is replaced with the hysteretic restoring force for the linear oscillator with 1-DOF NES. The hysteretic characteristics are described by the combination of the nonlinear cubic stiffness and the nonlinear hysteretic damping, which is depicted in Fig. 16. The nonlinear elastic restoring force remains consistent with k_{n2} , while the hysteretic damping is approximately expressed by elliptic characteristics. The major axis length and minor axis length are set to 0.3 and to 0.03, respectively, in this case. The other parameters remain equivalent to those of the linear oscillator in the 1-DOF NES case.

Figure 17 shows the results obtained by the proposed method and the COCO. A comparison of these two methods again demonstrates the accuracy of the improved DIHBM. As the hysteretic device is exerted on mass m_2 , which corresponds to the second resonance peak, the introduction of the hysteretic force

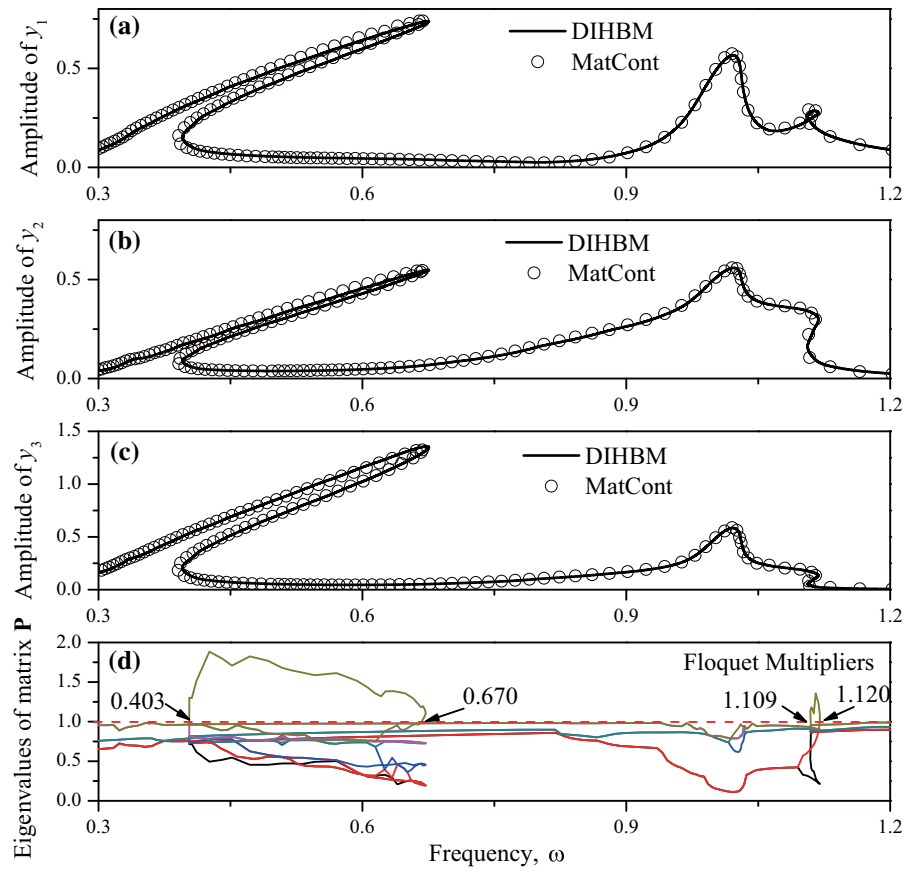


Fig. 15 Response diagram for a linear oscillator with 2-DOF NES: **a** frequency response curve of amplitude of y_1 ; **b** frequency response curve of amplitude of y_2 ; **c** frequency response curve of

amplitude of y_3 ; **d** eigenvalues of the monodromy matrix \mathbf{P} compared with ω

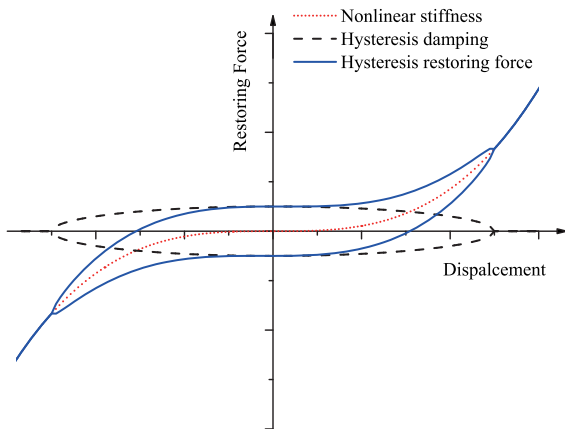


Fig. 16 Nonlinear elastic restoring force and hysteretic damping force

has an effect on decreasing the amplitude around the second resonance peak of both DOFs.

5 Conclusion

Based on the work by Wang [33], this paper extends the improved IHBM to the nonlinear damping system. This method is indicated to be efficient for obtaining the dynamics of both nonlinear stiffness systems and nonlinear damping systems. Compared with the traditional IHBM, it establishes a simpler and more general algorithm for the analysis of nonlinear vibration characteristics, promotes applications of IHBM in nonlinear damping systems.

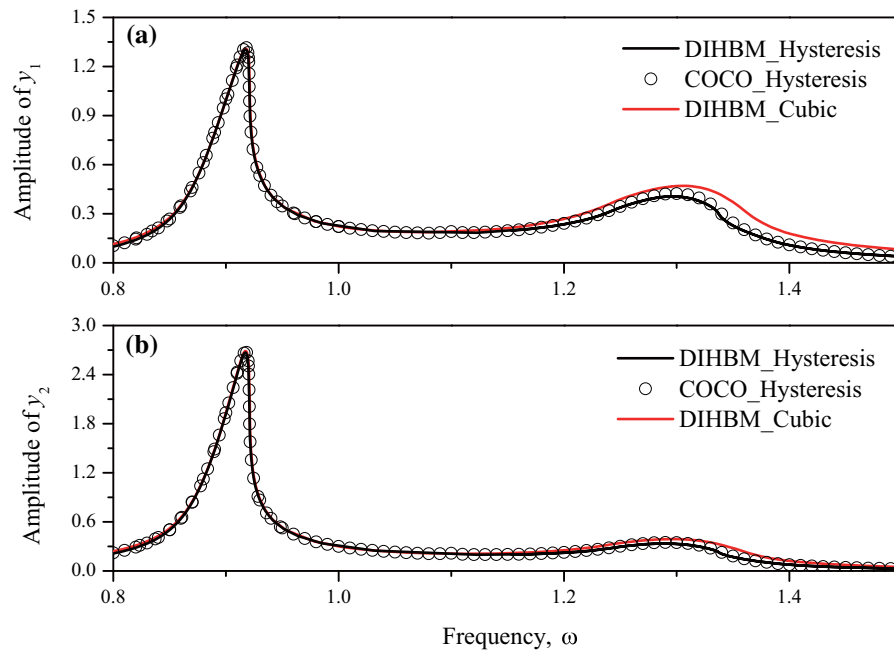


Fig. 17 Response diagram for the linear oscillator with different nonlinear stiffness types of the 1-DOF NES: **a** frequency response curve of amplitude of y_1 ; **b** frequency response curve of amplitude of y_2

The discrete node process for nonlinear damping systems is introduced to convert nonlinear systems with piecewise-linear systems, and the IHBM procedure for these piecewise-linearized damping systems, together with the stability of the solutions, is investigated. A quantified equivalent piecewise-linearization error process is proposed to meet the requirements of the veracity of the proposed method. A nonlinear polynomial damping system is selected to validate the proposed method by computing the dynamics of the system. The results show that the linearized error, which reaches approximately 1.4×10^{-3} , is applicable for analyzing nonlinear damping systems within the preset 5% error value. Five nonlinear damping SDOF systems are investigated. The results prove the accuracy of the improved method. Additionally, Two MDOF nonlinear systems are employed to demonstrate the extendibility of the proposed method.

Furthermore, the proposed method can expand its research in the displacement velocity-dependent isolators in further studies.

Funding There is no available fundings for this paper.

Data availability The datasets analyzed during the current study are available from the corresponding author on reasonable request.

Declarations

Conflict of interest We have no competing interests. All authors gave final approval for publication and agree to be accountable for all aspects of the work presented herein.

Human and animal rights No human or animal subjects were used in this work.

References

1. Karlii, D., Caji, M., Paunovi, S., et al.: Nonlinear energy harvester with coupled Duffing oscillators. *Commun. Nonlinear Sci.* **91**, 105394 (2020)
2. Ranjbarzadeh, H., Kakavand, F.: Determination of nonlinear vibration of 2DOF system with an asymmetric piecewise-linear compression spring using incremental harmonic balance method. *Eur. J. Mech. A Solids*. **73**, 161–168 (2019)
3. Kong, X., Sun, W., Wang, B., et al.: Dynamic and stability analysis of the linear guide with time-varying, piecewise-nonlinear stiffness by multi-term incremental harmonic balance method. *J. Sound Vib.* **346**, 265–283 (2015)
4. Sun, X., Jing, X.: A nonlinear vibration isolator achieving high-static-low-dynamic stiffness and tunable anti-resonance frequency band. *Mech. Syst. Signal Process.* **80**, 166–188 (2016)
5. Gao, X., Teng, H.-D.: Dynamics and nonlinear effects of a compact near-zero frequency vibration isolator with HSLD stiffness and fluid damping enhancement. *Int. J. Nonlin Mech.* **128**, 103632 (2021)

6. Wang, S., Hua, L., Yang, C., et al.: Nonlinear vibrations of a piecewise-linear quarter-car truck model by incremental harmonic balance method. *Nonlinear Dyn.* **92**, 1719–1732 (2018)
7. Ghandchi, T.-M., Elliott, S.-J.: Extending the dynamic range of an energy harvester using nonlinear damping. *J. Sound Vib.* **333**, 623–629 (2014)
8. Xiao, Z., Zhao, J., et al.: The transmissibility of vibration isolators with cubic nonlinear damping under both force and base excitations. *J. Sound Vib.* **332**, 1335–1354 (2013)
9. Habib, G., Cirillo, G.-I., Kerschen, G.: Isolated resonances and nonlinear damping. *Nonlinear Dyn.* **93**, 979–994 (2018)
10. Huang, X., Sun, J., Hua, H., et al.: The isolation performance of vibration systems with general velocity-displacement-dependent nonlinear damping under base excitation: numerical and experimental study. *Nonlinear Dyn.* **85**, 777–796 (2016)
11. Pierre, C., Ferri, A.-A., Dowell, E.-H.: Multi-harmonic analysis of dry friction damped systems using an incremental harmonic balance method. *J. Appl. Mech.* **52**, 958–964 (1985)
12. Niknam, A., Farhang, K.: Friction-induced vibration in a two-mass damped system. *J. Sound Vib.* **456**, 454–475 (2019)
13. Pesek, L., Pust, L., Snabl, P., Bula, V., Hajzman, M., Byrtus, M.: Dry-friction damping in vibrating systems, theory and application to the bladed disc assembly. In: Jauregui, J. (ed.) *Nonlinear Structural Dynamics and Damping. Mechanisms and Machine Science*, vol. 69. Springer, Cham (2019)
14. Hui, Y., Law, S.-S., Zhu, W., et al.: Extended IHB method for dynamic analysis of structures with geometrical and material nonlinearities. *Eng. Struct.* **205**, 1–14 (2020)
15. Vaiana, N., Sessa, S., Marmo, F., et al.: A class of uniaxial phenomenological models for simulating hysteretic phenomena in rate-independent mechanical systems and materials. *Nonlinear Dyn.* **93**, 1647–1669 (2018)
16. Vaiana, N., Sessa, S., Rosati, L.: A generalized class of uniaxial rate-independent models for simulating asymmetric mechanical hysteresis phenomena. *Mech. Syst. Signal Process.* **146**, 106984 (2021)
17. Caughey, T.-K.: Sinusoidal excitation of a system with bilinear hysteresis. *J. Appl. Mech.* **27**, 640–643 (1960)
18. Kalmárnagy, T., Shekhawat, A.: Nonlinear dynamics of oscillators with bilinear hysteresis and sinusoidal excitation. *Phys. D* **238**, 1768–1786 (2009)
19. Balasubramanian, P., Franchini, G., Ferrari, G., et al.: Nonlinear vibrations of beams with bilinear hysteresis at supports: interpretation of experimental results. *J. Sound Vib.* **499**, 115998 (2021)
20. Wong, C.-W., Ni, Y.-Q., Lau, S.-L.: Steady-state oscillation of hysteretic differential model. I. *J. Eng. Mech.* **120**, 2271–2298 (1994)
21. Wong, C.-W., Ni, Y.-Q., Ko, J.-M.: Steady-state oscillation of hysteretic differential model. II. *J. Eng. Mech.* **120**, 2299–2325 (1994)
22. Jalali, H.: An alternative linearization approach applicable to hysteretic systems. *Commun. Nonlinear Sci.* **19**, 245–257 (2014)
23. Civera, M., Grivet-talocia, S., Surace, C., et al.: A generalised power-law formulation for the modelling of damping and stiffness nonlinearities. *Mech. Syst. Signal Process.* **153**, 107531 (2021)
24. Miguel, L.-P.: Some practical regards on the application of the harmonic balance method for hysteresis models. *Mech. Syst. Signal Process.* **143**, 106842 (2020)
25. Zucca, S., Fitrone, C.-M.: Nonlinear dynamics of mechanical systems with friction contacts: coupled static and dynamic Multi-Harmonic Balance Method and multiple solutions. *J. Sound Vib.* **333**, 916–926 (2014)
26. Cheung, Y.-K., Chen, S.-H., Lau, S.-L.: Application of the incremental harmonic balance method to cubic non-linearity systems. *J. Sound Vib.* **140**, 273–286 (1990)
27. Zhang, Z., Tian, X., Ge, X.: Dynamic characteristics of the Bouc-Wen nonlinear isolation system. *Appl. Sci.* **11**, 6106 (2021)
28. Fang, L., Wang, J., Tan, X.: An incremental harmonic balance-based approach for harmonic analysis of closed-loop systems with Prandtl-Ishlinskii operator. *Automatica* **88**, 48–56 (2018)
29. Xiong, H., Kong, X., Li, H., et al.: Vibration analysis of nonlinear systems with the bilinear hysteretic oscillator by using incremental harmonic balance method. *Commun. Nonlinear Sci.* **42**, 437–450 (2017)
30. Wang, X.-F., Zhu, W.-D.: A modified incremental harmonic balance method based on the fast Fourier transform and Broyden's method. *Nonlinear Dyn.* **81**, 981–989 (2015)
31. Sun, M.: Effect of negative stiffness mechanism in a vibration isolator with asymmetric and high-static-low-dynamic stiffness. *Mech. Syst. Signal Process.* **124**, 388–407 (2019)
32. Hui, Y., Law, S.-S., Zhu, W., et al.: Internal resonance of structure with hysteretic base-isolation and its application for seismic mitigation. *Eng. Struct.* **229**, 111643 (2021)
33. Wang, S., Hua, L., Yang, C., et al.: Applications of incremental harmonic balance method combined with equivalent piecewise-linearization on vibrations of nonlinear stiffness systems. *J. Sound Vib.* **441**, 111–125 (2019)
34. Lau, S.-L.: Nonlinear vibrations of piecewise-linear systems by incremental harmonic balance method. *J. Appl. Mech.* **59**, 153–160 (1992)
35. Dhooge, A., Govaerts, W., Kouznetsov, Y.A., et al.: New features of the software MatCont for bifurcation analysis of dynamical systems. *Math. Comput. Model. Dyn.* **14**, 1–18 (2008)
36. Dankowicz, H., Schilder, F.: *Recipes for Continuation*. SIAM, New Delhi (2013)
37. Teloli, R.D., da Silva, S.: A new way for harmonic probing of hysteretic systems through nonlinear smooth operators. *Mech. Syst. Signal Process.* **121**, 856–875 (2019)
38. Okuizumi, N., Kimura, K.: Multiple time scale analysis of hysteretic systems subjected to harmonic excitation. *J. Sound Vib.* **272**, 675–701 (2004)
39. Carpineto, N., Lacarbonara, L., et al.: Hysteretic tuned mass dampers for structural vibration mitigation. *J. Sound Vib.* **333**, 1302–1318 (2014)

40. Zhang, Y., Kong, X., Yue, C., et al.: Dynamic analysis of 1-dof and 2-dof nonlinear energy sink with geometrically nonlinear damping and combined stiffness. *Nonlinear Dyn.* **105**, 167–190 (2021)
41. Zhang, Y., Spanos, P.-D.: Efficient response determination of a M-D-O-F gear model subject to combined periodic and stochastic excitations. *Int. J. Nonlinear Mech.* **120**, 103378 (2020)

Publisher's Note Springer Nature remains neutral with regard to jurisdictional claims in published maps and institutional affiliations.